

## Finite element models of reinforced ECC beams subjected to various cyclic deformation

Timothy E. Frank<sup>\*1</sup>, Michael D. Lepech<sup>2a</sup> and Sarah L. Billington<sup>2b</sup>

<sup>1</sup>Headquarters Air Force, 1260 Air Force Pentagon, Washington, DC 20330, USA

<sup>2</sup>Department of Civil and Environmental Engineering, Stanford University, 473 Via Ortega, Stanford, CA 94305, USA

(Received July 25, 2017, Revised July 29, 2018, Accepted August 31, 2018)

**Abstract.** Steel reinforced Engineered Cementitious Composite (ECC) components have been proposed for seismic structural applications, for example in coupling beams, infill panels, joints, columns, and flexural members. The development of strain in the steel reinforcement of cementitious components has been shown to vary based on both the steel reinforcement ratio and the applied deformation history. Strain in the steel reinforcement of reinforced ECC components is an important structural response metric because ultimate failure is often by fracture of the steel reinforcement. A recently proposed bond-slip model has been successfully calibrated to cyclically tested reinforced ECC beams wherein the deformation history contained monotonically increasing cycles. This paper reports simulations of two-dimensional finite element models of reinforced ECC beams to determine the appropriateness and significance of altering a phenomenological bond-slip model based on the applied deformation history. The numerical simulations with various values of post-peak bond-slip softening stiffness are compared to experimental results. Varying the post-peak bond-slip softening stiffness had little effect on the cracking patterns and hysteretic response of the reinforced ECC flexural models tested, which consisted of two different steel reinforcement ratios subjected to two different deformation histories. Varying the post-peak bond-slip softening stiffness did, however, affect the magnitude of strain and the length of reinforcing bar that strain-hardened. Overall, a numerical model with a constant bond-slip model represented well various responses in reinforced ECC beams with multiple steel reinforcement ratios subjected to different deformation histories.

**Keywords:** Engineered Cementitious Composite (ECC); cyclic deformation history; steel reinforcement strain; bond-slip model; 2D finite elements

### 1. Introduction and motivation

Engineered Cementitious Composite (ECC) materials belong to the class of High-Performance Fiber-Reinforced Cement-based Composites (HPFRCCs), and are made using short, randomly dispersed polymeric fibers in a mortar mixture. Under uniaxial tension, ECC forms microcracks and experiences enhanced specimen ductility over traditional mortar or concrete through a phenomenon referred to as pseudo-strain hardening (Maalej and Li 1995). Reinforced ECC has been proposed for a number of different structural applications, including improving performance under seismic loading (Li and Kanda 1998).

Recent research has modeled the response of structural components subjected to cyclic loading and observed improvement by incorporating bond-slip between the steel reinforcing bar and the cementitious material. Prescribing an interface layer to facilitate bond-slip has been shown to accurately capture structural stiffness in simulations of

reinforced concrete beam-column joints (Kwak and Filippou 1990) and cracking patterns in reinforced ECC beams (Bandelt 2015). Bandelt and Billington (2016a) developed a phenomenological bond-slip model and calibrated it using results from reinforced ECC beam experiments. The model is phenomenological in that it accounts for reductions in bond strength due to both splitting cracks and interface crushing, as both were observed in the experimental results to which the model was calibrated. The bond-slip model was extended to facilitate cyclic loading and developed for use with zero-thickness interface elements in a DIANA (DIplacement ANALyzer) finite element model (Bandelt 2015). Three dimensional numerical simulations have shown splitting and interface crushing in line with experimental ECC bond-slip experiments (Bandelt *et al.* 2017).

Though earthquakes can generate many different deformation histories in structures, to date only cyclic deformation histories with monotonically increasing cycles have been applied in numerical simulations of reinforced ECC beams using a bond-slip model. A recent study of reinforced ECC beams of various steel reinforcement ratios subjected to cyclic loading indicated the maximum drift at fracture increased with increasing steel reinforcement ratio (Bandelt and Billington 2016b). Other studies demonstrated that sensitivity to deformation history of reinforced ECC beams varied with steel reinforcement ratio (Frank *et al.*

---

\*Corresponding author, Ph.D.

E-mail: [timothy.frank@us.af.mil](mailto:timothy.frank@us.af.mil)

<sup>a</sup>Ph.D.

E-mail: [mlepech@stanford.edu](mailto:mlepech@stanford.edu)

<sup>b</sup>Ph.D.

E-mail: [billingt@stanford.edu](mailto:billingt@stanford.edu)

2017, Frank *et al.* 2018).

This study uses two-dimensional finite element models of reinforced ECC beams to determine if and how a bond-slip model should be adjusted based on applied deformation history or steel reinforcement ratio to accurately capture response parameters of cracking, hysteresis, and failure. The primary variable explored within the bond-slip model was the post-peak bond-slip softening stiffness parameter,  $k$ , due to both numerical and experimental observations in previous studies. Bandelt (2015), observed a sensitivity to differing simulated response upon altering  $k$  when modeling reinforced ECC beams. Experimental observations of cyclically loaded reinforced ECC beams showed that the applied deformation history was a good indicator of the abrupt or gradual nature of strain reductions in the steel reinforcing bars at relatively large levels of drift (Frank 2017). Because formation of splitting cracks was observed differently in specimens subjected to different deformation histories, modifying the parameter,  $k$ , was expected to directly control how abrupt or gradual the simulated post-peak strain reductions would be.

Two-dimensional finite element models of reinforced ECC components of two different steel reinforcement ratios, 0.95% and 0.73%, were built and subjected to simulated cyclic loading. Models were then subjected to two different cyclic deformation histories, and a sensitivity analysis was conducted on the post-peak bond-slip softening stiffness parameter of the bond-slip model leaving all other material and model properties constant. The ability of the numerical simulations to capture response of reinforced ECC flexural members subjected to different cyclic deformation histories was assessed by observing cracking patterns, hysteretic response, and strain in the steel reinforcing bars.

## 2. Finite element model geometry and constitutive model

### 2.1 Reinforced ECC specimens with a 0.95% steel reinforcement ratio

Multiple approaches have been employed in numerical simulations of cementitious materials. A discrete crack approach, which explicitly models each crack, has been used, though this method is computationally intensive (Hung and El-Tawil 2010). In fiber-reinforced composites, discretely modeling each fiber or using an embedded formulation for the fibers has been successfully implemented (Cunha *et al.* 2012, Radtke *et al.* 2010). These approaches have facilitated a better understanding of the effects of fiber orientation at the material level. For component modeling at the structural level, however, it is more common to use a smeared crack approach, wherein the response of the fibrous HPFRCC matrix is represented by the constitutive laws assigned to the element, and elements crack when the principal tensile strain exceeds user-defined cracking strain at an integration point.

In the smeared crack approach, the presence of a crack is simulated by a modification to local material properties. Modification to the local material properties can be done in

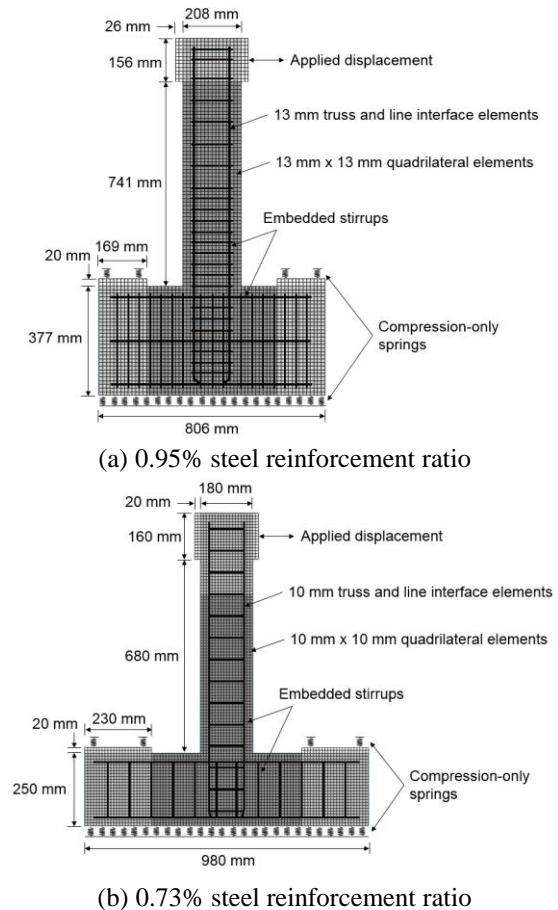


Fig. 1 Model geometries for reinforced ECC specimens

one of two primary ways: through 1) a rotating crack model or 2) a fixed crack model. The fixed crack approach for cyclic simulations of reinforced ECC beam models was used in several studies (Kaufmann and Marti 1998, Han *et al.* 2003, Stavridis and Shing 2010, Bandelt 2015). A fixed crack formulation was used in this study after preliminary investigations showed a fixed crack approach resulted in more representative hysteretic results than a rotating crack approach.

Finite element models were constructed to represent two experimental specimens reported in Frank (2017): ECC-0.95-F and ECC-0.95-LP. The specimen geometry is a vertical cantilever with an enlarged base clamped to a strong floor, and the numerical model geometry is shown in Fig. 1(a). The ECC and steel plates were modeled with eight-noded 13 mm×13 mm plane stress elements. The ECC was modeled using a total strain based fixed crack model in tension, and a total strain based parabolic model in compression. Elements were 165 mm thick in the beam and 229 mm thick in the enlarged base and steel plates. A three by three Gaussian integration scheme was used for the eight-noded elements. The steel reinforcement was modeled with two-noded 13 mm long truss elements that were directly integrated. The 0.95% flexural steel reinforcement ratio, provided by two 13 mm diameter bars, was modeled with a total cross-sectional area of 253 mm<sup>2</sup> and a perimeter of 79.8 mm. The transverse steel was modeled as perfectly bonded, embedded reinforcement in the eight-noded ECC

elements. The bond-slip behavior between the longitudinal steel reinforcement and ECC was modeled with four-noded 13 mm long interface elements with zero thickness. A two-point Newton-Coates integration scheme was used for the interface elements.

The steel supporting the specimen was modeled as a compression-only elastic foundation with stiffness of  $9 \times 10^5$  N/mm at each node in order to replicate experimental conditions. The base of the specimen was restrained from lateral displacement. Threaded rods clamping the ends of the enlarged base between the steel plates and the supporting steel underneath the specimen were modeled as compression-only springs with a stiffness of  $1 \times 10^4$  N/mm to represent the geometry and material properties of the rods.

### 2.2 Reinforced ECC specimens with a 0.73% steel reinforcement ratio

Finite element models were also constructed of experimental specimens ECC-0.73-F and ECC-0.73-LP, as reported in Frank (2017). Because the geometry between specimens reinforced to 0.95% and 0.73% were different, the numerical models also differed. For specimens reinforced to a 0.73% steel reinforcement ratio, the ECC and steel plates were modeled with eight-noded 10 mm × 10 mm plane stress elements (Fig. 1(b)) The ECC was modeled using a total strain based fixed crack model in tension, and a total strain based parabolic model in compression. The steel reinforcement and interface element lengths were also 10 mm to match the length of the ECC elements. Element thickness was 127 mm in all members. The 0.73% steel reinforcement ratio in flexure, provided by two 10 mm diameter bars, was modeled with a total cross-sectional area of 143 mm<sup>2</sup> and a perimeter of 59.8 mm. Threaded rods clamping the ends of the specimens with a 0.73% steel reinforcement ratio were modeled as compression-only springs with a stiffness of  $6 \times 10^5$  N/mm to represent experimental geometry and properties.

## 3. Description of simulations

### 3.1 Material properties and model parameters

Material properties and model parameters are shown in Table 1. They were selected based on values used in previous numerical studies or the results of compressive cylinder and third-point bending tests, as reported in Frank (2017). Initial tensile strength ( $f_t$ ), cracking strain ( $\varepsilon_{to}$ ), Young's modulus ( $E$ ), and fracture energy ( $G_f$ ) of the ECC were estimated from an inverse analysis (Soranakom and Mobasher 2007) using the nonlinear finite element software DIANA wherein a multi-linear material model was assumed. Model parameters were altered until the simulated equivalent bending stress curve aligned with experimental results of four monotonic third point bending tests of 80 mm × 80 mm × 305 mm ECC beams.

Tensile strength and tensile fracture energy were reduced by 10% and 50%, respectively, for all simulations per the approach proposed in Bandelt (2015) to account for damage due to cyclic loading for each of the simulations. A

Table 1 2D Material properties and model parameters

ECC			
Variable	Description	Value	Units
$E$	Young's modulus	7.0	GPa
$f'_c$	Compressive strength	46	MPa
$G_c$	Compressive fracture energy	52.5	MPa-mm
$\varepsilon_{to}$	Cracking strain	0.000514	mm/mm
$f_t$	Tensile strength	3.6	MPa
$\sigma_{tp}$	Stress at onset of softening	3.6	MPa
$\varepsilon_{tp}$	Strain at onset of softening	0.011	mm/mm
$G_f$	Tensile fracture energy	2.3	MPa-mm
$\nu$	Poisson's ratio	0.15	--
$\beta$	Shear retention factor	0.01	--
13 mm Longitudinal steel			
$E$	Young's modulus	200	GPa
$F_y$	Yield strength	455	MPa
$F_u$	Ultimate strength	675	MPa
$\varepsilon_{sh}$	Strain at onset of strain hardening	0.014	mm/mm
$\varepsilon_u$	Strain at fracture	0.18	mm/mm
$\nu$	Poisson's ratio	0.3	--
10 mm Longitudinal steel			
$E$	Young's modulus	200	GPa
$F_y$	Yield strength	445	MPa
$F_u$	Ultimate strength	690	MPa
$\varepsilon_{sh}$	Strain at onset of strain hardening	0.014	mm/mm
$\varepsilon_u$	Strain at fracture	0.16	mm/mm
$\nu$	Poisson's ratio	0.3	--
Transverse steel			
$E$	Young's modulus	200	GPa
$F_y$	Yield strength	690	MPa
$\nu$	Poisson's ratio	0.3	--

thorough sensitivity analysis of the effect on cracking, hysteresis, bond-slip, and strain in the reinforcement when adjusting tensile fracture energy and tensile strength can be found in Bandelt (2015). The strain at total softening,  $\varepsilon_{tu}$ , was determined as a function of the finite element mesh size to eliminate mesh dependency as described by Hung and El-Tawil (2010). Using the 50% reduced fracture energy,  $\varepsilon_{tu}$  was calculated per Eq. (1), where  $G_f$  is the tensile fracture energy,  $h$  is the square root of the element area,  $\sigma_{tp}$  is the stress at the onset of softening, and  $\varepsilon_{tp}$  is strain at the onset of softening.

$$\varepsilon_{tu} = 2 \frac{G_f}{h} \frac{1}{\sigma_{tp}} + \varepsilon_{tp} \quad (1)$$

The compressive fracture energy was 52.5 MPa-mm from experimental results of the same ECC material (Moreno-Luna 2014), and the compressive strength was determined from experimental results of four 100 mm × 200 mm cylinder tests as reported in Frank (2017). Poisson's ratio of the ECC was 0.15 (Moreno *et al.* 2014). A constant

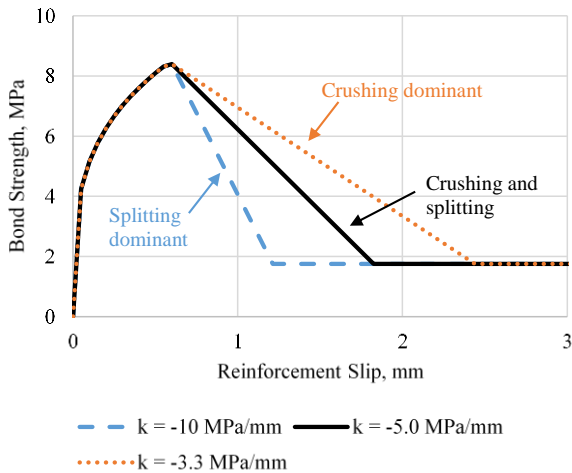


Fig. 2 Bond-slip models used in 2D numerical simulations of beam-end models

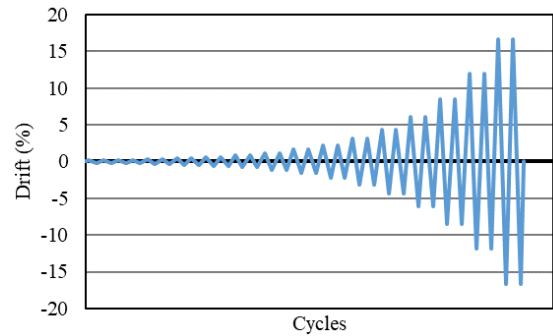
shear retention factor was assumed to be 0.01 (Bandelt 2015).

Young's modulus of the steel reinforcement was 200 GPa, based on experimental testing. Yield strength, strain at the onset of strain hardening, and ultimate strength of steel were determined experimentally as reported in Frank (2017). Cyclic behavior, which included the Bauschinger effect, was governed by a set of rules calibrated through experimental results and described in Shen *et al.* (1993).

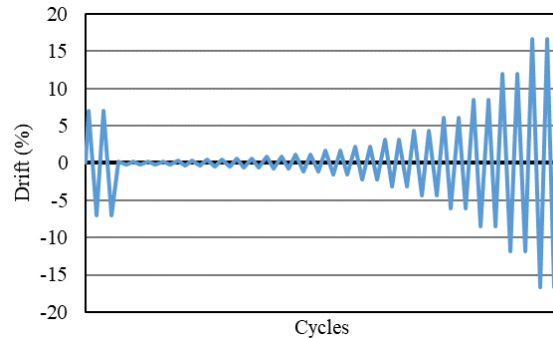
The framework for the bond-slip interface model used in this study was proposed by Bandelt (2015). The inclusion of bond-slip in reinforced ECC flexural component simulations was important to accurately represent cracking patterns, hysteretic behavior, and to predict fracture of the steel reinforcement. The recommended value of the post-peak bond-slip softening stiffness,  $k$ , for cyclic loading of reinforced ECC components with the same mixture design of  $-5.0$  MPa/mm was adopted. This recommendation was validated on specimens that experienced splitting cracks, which was the case with the specimens being modeled here.

The mechanism or mechanisms leading to debonding and subsequent reduction in reinforcement strain are closely related to the bond-slip behavior. Results from Frank (2017) suggested specimens that formed splitting cracks often incurred an abrupt reduction in strain of the steel reinforcement. An abrupt steel strain reduction is associated with a steeper softening branch of the cyclic bond-slip envelope, wherein a small increase in reinforcement slip past peak strength induces a relatively large decrease in bond strength (Fig. 2 "Splitting dominant" curve).

Results from Frank (2017) also indicated, regardless of the presence of splitting cracks at the conclusion of the test, a cyclic deformation history with monotonically increasing cyclic amplitudes and no initial pulses, was more likely to induce reinforcement strain reductions due to interface crushing than due to the splitting cracks themselves. Strain reductions due to interface crushing were shown to be more gradual, and less abrupt than strain reductions due to splitting cracks. A more gradual reduction in strain may be associated by a less steep softening branch of the cyclic bond-slip envelope, wherein crushing facilitates slip in



(a) FEMA



(b) Large pulse

Fig. 3 Deformation histories

conjunction with a modest decrease in bond strength (Fig. 2 "Crushing dominant" curve).

Thus, simulations herein used three value of post-peak bond-slip stiffness,  $k$ :  $-5.0$  MPa/mm,  $-10$  MPa/mm, and  $-3.3$  MPa/mm. Numerical results were compared to each other and to experimental results from Frank (2017) to evaluate the bond-slip model in conjunction with specimens with various steel reinforcement ratios subjected to various deformation histories. The peak bond strength and residual friction bond strength were kept constant at 7.87 MPa and 1.75 MPa, respectively, for all simulations per recommendations by Bandelt (2015).

#### 4. Simulation program and nonlinear analysis approach

Two deformation histories were used in this study. The deformation history proposed in FEMA 461 (2007), hereafter referred to as the 'FEMA' deformation history, was composed of two cycles per amplitude step; each step 40% larger in amplitude than the previous one (Fig. 3(a)). The first amplitude step was 0.15% drift, where drift was calculated as the horizontal deflection at the point of loading divided by the span length (760 mm for specimens reinforced to 0.73% or 819 mm for specimens reinforced to 0.95%). The second deformation history used in this study began with two initial pulses to either 5.5% or 7% drift that preceded the FEMA deformation history, called the 'Large Pulse' (LP) deformation history (e.g., Fig. 3(b)). Due to preliminary experimental monotonic testing of reinforced ECC beams, 5.5% and 7% drift were chosen as the initial

Table 2 Simulation naming convention

Simulation name	Reinforcement ratio, %	Deformation history	Post-peak bond-slip softening stiffness, $k$ , MPa/mm
0.95-F-5	0.95	FEMA	-5.0
0.95-F-3	0.95	FEMA	-3.3
0.95-LP-5	0.95	Large Pulse	-5.0
0.95-LP-10	0.95	Large Pulse	-10
0.73-F-5	0.73	FEMA	-5.0
0.73-F-3	0.73	FEMA	-3.3
0.73-LP-5	0.73	Large Pulse	-5.0
0.73-LP-10	0.73	Large Pulse	-10

pulse amplitudes for specimens reinforced to 0.73% and 0.95% steel reinforcement ratio, respectively, based on 45% of ultimate drift at fracture.

Simulations were conducted up to the ultimate drift of the corresponding experimental test as reported in Frank (2017). For each steel reinforcement ratio and deformation history, a bond-slip model with  $k=-5.0$  MPa/mm was simulated as a control. For models subjected to the FEMA deformation history, a second simulation using  $k=-3.3$  MPa/mm was also used to simulate crushing dominant behavior, or a less abrupt strain reduction in the steel reinforcing bar at large levels of bar slip. The post-peak area under the bond-slip curve, or bond toughness, when  $k=-3.3$  MPa/mm was 50% larger than when  $k=-5.0$  MPa/mm. For models subjected the Large Pulse (LP) deformation history, a second simulation using  $k=-10$  MPa/mm was carried out to capture splitting dominant behavior, or a more abrupt strain reduction in the steel reinforcing bar at large levels of bar slip. The bond toughness when  $k=-10$  MPa/mm was 50% smaller than when  $k=-5.0$  MPa/mm. An increase in bond toughness of 300% between a pull-out (interface crushing) failure and a splitting failure is within the range of what may be expected in reinforced ECC based on Harajli *et al.* (2002).

Table 2 shows a summary of the two-dimensional simulations carried out in this study including details about the steel reinforcement ratio, deformation history, and bond-slip interface parameters. The naming convention of the simulations includes the steel reinforcement ratio (either 0.95% or 0.73%), the deformation history (either FEMA or Large Pulse), and the absolute value of the post-peak bond-slip softening stiffness. Each of four experimental specimens in Frank (2017) were modeled with two numerical simulations. For example, experimental specimen ECC-0.95-F was the impetus for simulations 0.95-F-5 and 0.95-F-3.

Simulations were carried out using the nonlinear finite element software DIANA version 9.6. A step size of between 0.15 and 0.25 mm with a Newton-Raphson iteration scheme was used. A line search algorithm was used to aid in the iterative scheme. Convergence was achieved when at least one of the force, displacement, or energy norms were less than or equal to 1%, 0.1% or 0.01%, respectively.

## 5. Simulation results

### 5.1 FEMA deformation history with $k=-5.0$ MPa/mm

#### 5.1.1 Cracking

The cracking strains at the peak drift (12% drift) in model 0.95-F-5 showed a dominant crack at the base of the beam as the ECC strain exceeded the strain at total softening,  $\epsilon_{tu}$  (Fig. 4(a)). The enlarged base remained linear elastic in the simulation as indicated by the tensile strain remaining below cracking strain,  $\epsilon_{to}$ . The ECC in the beam underwent multiple cracking, as indicated by tensile strain exceeding cracking strain extending about two-thirds up the height of the specimen, but remaining below the strain at the onset of softening,  $\epsilon_{tp}$ . Because many cracks on the compression side of the specimen had closed, high crack strains on only one side of the specimen are displayed in Fig. 4(a), but a similar cracking pattern on the opposite side was evident upon simulated excursions in the other direction. For comparison, the final cracking pattern of the associated experimental specimen, ECC-0.95-F (Fig. 4(b)), shows a similar cracking pattern to model 0.95-F-5, indicating the parameters and material properties of the simulation effectively captured the extent of cracking of the physical specimen.

The cracking response at peak drift (6.1% drift) of model 0.73-F-5 also aligned well with the associated experimental specimen, ECC-0.73-F (Fig. 4(c)). Because the specimen geometry of model 0.73-F-5 provided less steel reinforcement and lower confinement in the enlarged base than model 0.95-F-5, cracks formed in the joint. A dominant crack formed at the base of the beam and multiple cracks extended about two-thirds up the height of the specimen. The location and extent of multiple cracking and the presence and location of a dominant crack suggest cracking response of model 0.73-F-5 is in agreement with experiment ECC-0.73-F (Fig. 4(d)). The ability of the simulations to capture the cracking observed in experimental tests indicate that the ECC material properties in the numerical model well represent the ECC in the experimental specimens well.

#### 5.1.2 Hysteretic response

The simulated hysteretic responses of models 0.95-F-5 and 0.73-F-5 also were similar to the experimental response of specimens ECC-0.95-F and ECC-0.73-F, respectively (Fig. 5). Once a full-depth dominant crack formed, the response of the steel reinforcing bar dominated the overall response of the numerical model. The similarity of the hysteretic response, particularly at large drifts, between the models and their corresponding experiments indicate the material properties of the steel elements represent those in the steel reinforcing bars used in the experimental specimens well.

In general, models 0.95-F-5 and 0.73-F-5 underpredicted unloading and reloading stiffness, which generated narrower hysteresis loops in the simulations when compared to the experimental data. Narrower hysteresis loops resulted in an underprediction of energy dissipated by the test specimens, calculated as the area inside the hysteresis loops. Peak strength of model 0.95-F-5 was 10%

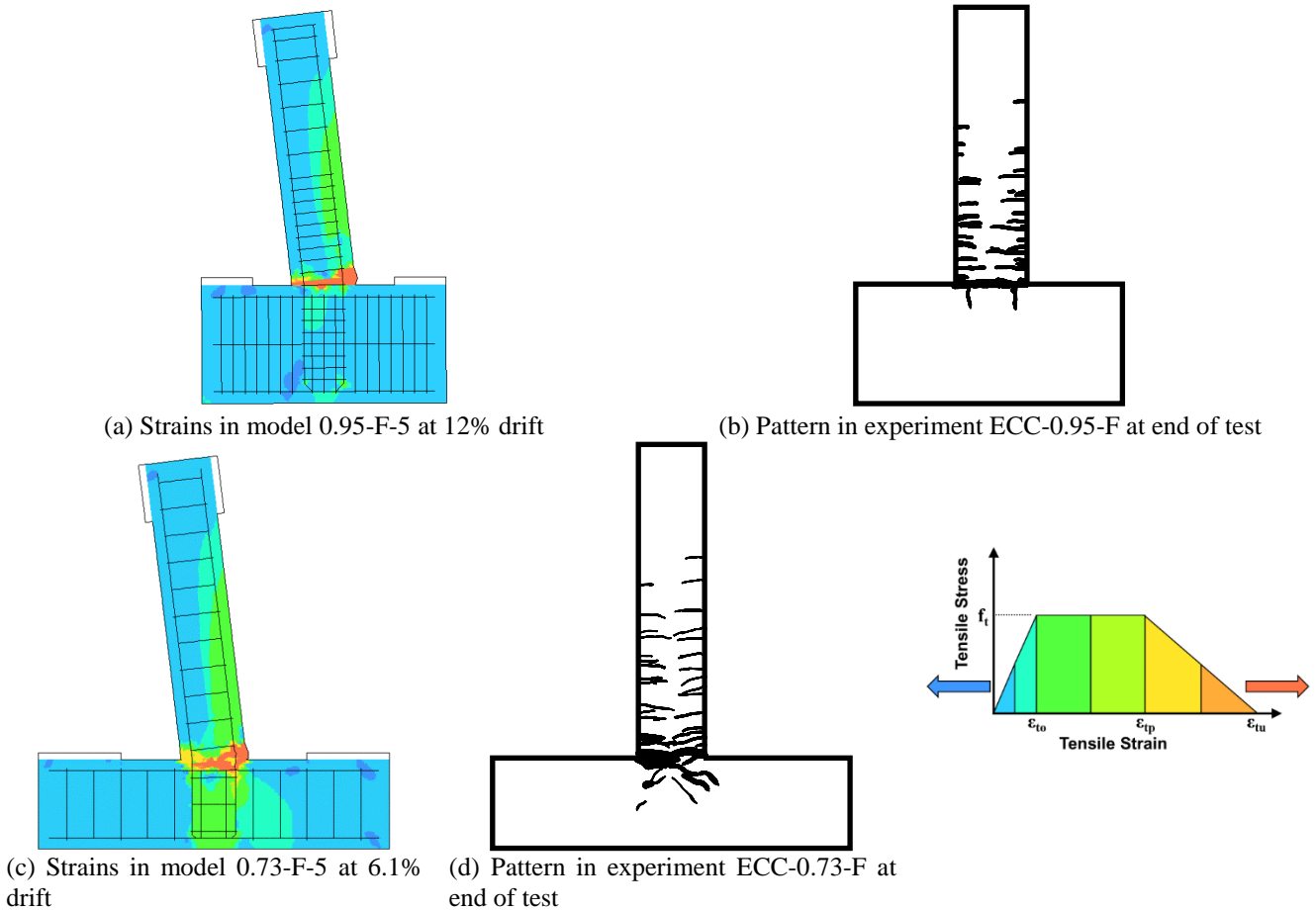


Fig. 4 Cracking

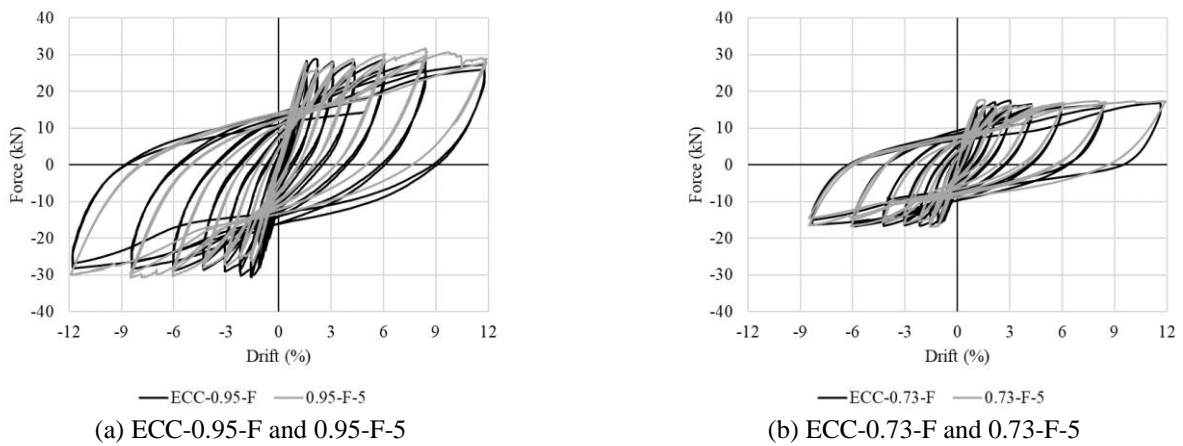


Fig. 5 Hysteretic response

higher than peak strength in ECC-0.95-F. The hysteresis envelopes show specimen strength at the peak of each excursion increased with drift in 0.95-F-5 through 8.5% drift, whereas specimen strength at the peak of each excursion decreased with increasing drift in the experiment (Fig. 5(a)). In model 0.95-F-5, the strain hardening of the steel reinforcing bar elements slightly outpaced the localized crushing of ECC elements that decreased the moment arm in the cross-section. The opposite trend occurred in the experimental specimen ECC-0.95-F. Energy dissipated by model 0.95-F-5 was 17% lower than that by

ECC-0.95-F through specimen failure. Peak strength of model 0.73-F-5 was essentially the same as the peak strength in ECC-0.73-F, and energy dissipated by model 0.73-F-5 was 16% lower than that by ECC-0.73-F (Fig. 5(b)).

5.1.3 Steel reinforcement strain

Another means of comparison between the numerical models and the experimental results was strain in the steel reinforcement. Using numerical models, strain in the steel reinforcement was recorded during simulations every 10

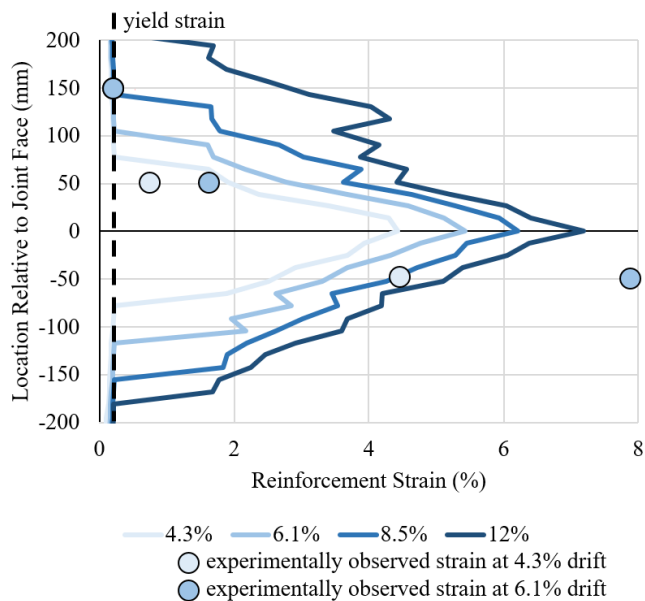


Fig. 6 Reinforcement strain profile in 0.95-F-5 and ECC-0.95-5

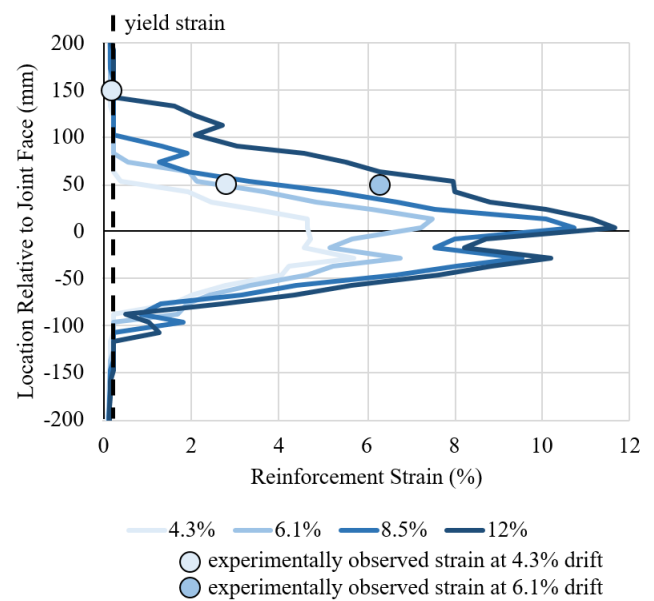


Fig. 7 Reinforcement strain profile in 0.73-F-5 and ECC-0.73-5

mm (for models containing a 0.73% steel reinforcement ratio) or 13 mm (for models containing a 0.95% steel reinforcement ratio) at locations where the nodes of the steel elements were connected to the corner nodes of the ECC elements through an interface element. The numerical simulations captured the strain in the steel reinforcement at many more points along the length of the steel reinforcement than the three experimental strain gages affixed to the steel reinforcing bars. However, the available strain gage data was investigated to validate the numerical simulations.

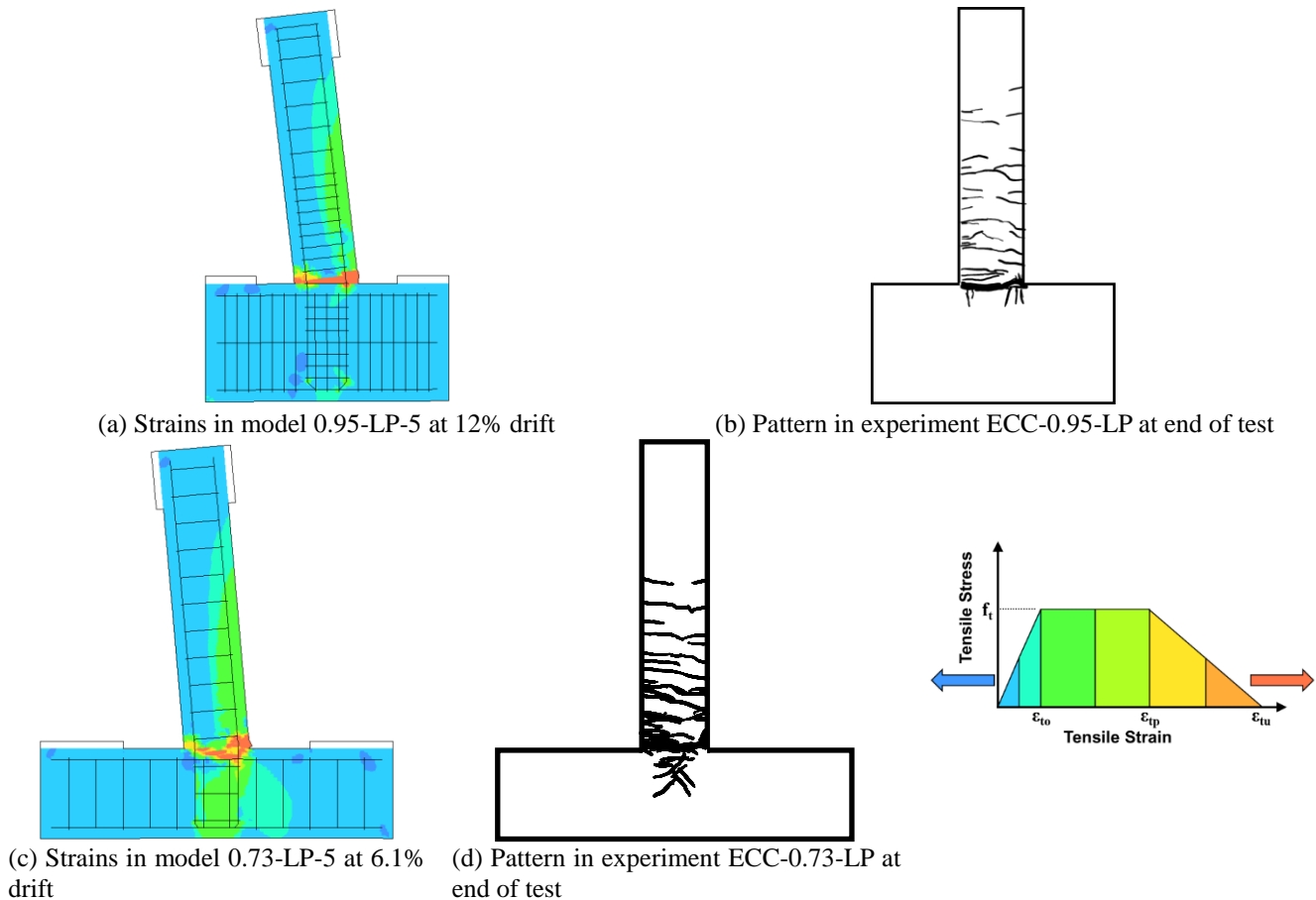
Fig. 6 shows reinforcement strain profiles of model 0.95-F-5 from 200 mm below to 200 mm above the joint face along the longitudinal steel bar elements in tension at the peak of the first excursion to four levels of drift: 4.3%, 6.1%, 8.5%, and 12%. Strain in the steel reinforcement was highest near the base of the beam where the applied moment was highest. Both the magnitude of strain and the length of reinforcing bar that underwent strain hardening increased with drift. Model 0.95-F-5 simulated the steel reinforcement strain located 150 mm above the joint remained at or below yield strain through 8.5% drift, which is in agreement with reinforcement strain experimentally observed in ECC-0.95-F at 6.1% drift, when the strain gage failed.

The magnitude of the reinforcement strains simulated by model 0.95-F-5 located 50 mm above and 50 mm below the joint face indicated agreement with experimentally observed strain gage data from ECC-0.95-F. While the magnitude of reinforcement strains located 50 mm above and below the joint face differed between 0.95-F-5 and ECC-0.95-F, differences may be, at least partially, explained by a 20 mm vertical shift in the location of the strain gage relative to the specimen joint as opposed to inaccuracies in the model (Fig. 6). Human error in attaching the strain gage, tying the steel reinforcement together, or casting the ECC, as well as irregularities in how the ECC cracked or

debonded from the steel are plausible reasons the experimental strain gage data may be shifted vertically relative to the strain profile generated as a result of the numerical simulation. For example, at 50 mm above the joint at 4.3% drift, reinforcement strain in ECC-0.95-F was 0.8%, while model 0.95-F-5 simulated reinforcement strain to be 2.0%. At 50 mm into the joint at 4.3% drift, reinforcement strain in ECC-0.95-F was 4.4%, while model 0.95-F-5 simulated reinforcement strain to be 2.6%. Overall, the trends in the simulated reinforcing bar strains were similar to measured strains from strain gages.

Fig. 7 shows reinforcement strain profiles of model 0.73-F-5 from 200 mm below to 200 mm above the joint face along the longitudinal steel bar elements in tension at the peak of the first excursion to four levels of drift: 4.3%, 6.1%, 8.5%, and 12%. Model 0.73-F-5 projected reinforcement strain at 150 mm above the joint remained at yield strain or lower through 4.3% drift, matching experimental observations in ECC-0.73-F. The strain gage at 50 mm into the joint failed early in the test and no data was recorded at or above the cycles to 4.3% drift. Similar to the observation between simulated and experimental data in Fig. 6, a vertical shift of about 25 mm lower towards the joint of the experimentally observed reinforcement strain data, as opposed to inaccuracies in the model, may account for the difference between observed and simulated reinforcement strain.

When comparing Fig. 6 to Fig. 7, simulated reinforcement strains in the steel elements were higher at a given drift when the steel reinforcement ratio and reinforcing bar size were lower. This increase in reinforcement strain with a decrease in reinforcement ratio reinforces one of the findings from Frank (2017); less reinforced specimens exhibited a larger bond-strength-to-bond-demand ratio, which limited debonding and encouraged strain accumulation in the steel reinforcement.



## 5.2 Large pulse deformation history with $k=-5.0$ MPa/mm

### 5.2.1 Cracking

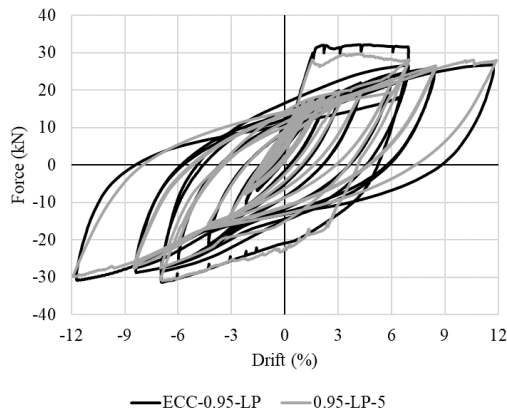
The presence and location of the dominant crack and the extent of multiple cracking along the height of specimen ECC-0.95-LP (Frank 2017) was well captured by model 0.95-LP-5 (Fig. 8(a)-(b)). Similarly, the cracking pattern of ECC-0.73-LP was well captured by 0.73-LP-5, wherein cracking in the enlarged base was also observed (Fig. 8(c)-(d)). Similar to the experiments and simulations mentioned in Section 5.1.1, because the specimen geometry of model 0.73-LP-5 provided less steel reinforcement and lower confinement in the enlarged base than 0.95-LP-5, cracks formed in the joint.

### 5.2.2 Hysteretic response

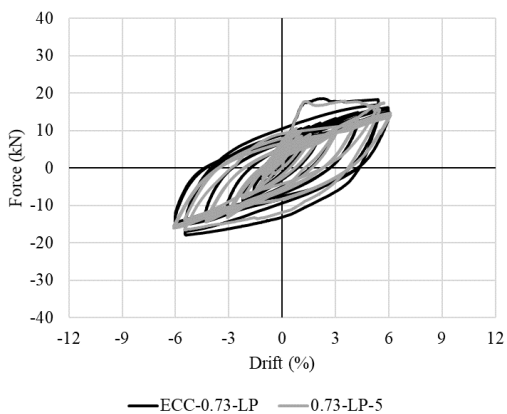
Model 0.95-LP-5, with a 0.95% steel reinforcement ratio, had a post-peak bond-slip softening stiffness of  $-5.0$  MPa/mm, and was subjected to the LP deformation history. The model's peak strength, pinching due to reduced reloading stiffness, and total energy dissipated indicated agreement with the associated experiments (Fig. 9(a)). Peak strength of model 0.95-LP-5 was 7.4% less than ECC-0.95-F. Though tested quasi-statically, relaxation of about 5% in specimen strength was observed during pauses in the test, as photographs and measurements were taken. Relaxation, attributed to ECC cracking and steel yielding (similar to

reinforced concrete specimens reported by Leon and Deierlein 1996), or slight differences in the placement of the reinforcing bars during casting are both plausible explanations for the 7.4% difference between numerical and experimental specimen strengths. Reloading stiffness and pinching behavior of model 0.95-LP-5 were similar, yet the hysteresis loops were not as wide as ECC-0.95-LP. The total energy dissipated by model 0.95-LP-5 was 14% less than that of ECC-0.95-LP through the conclusion of testing (Fig. 9(a)).

Similar to model 0.95-LP-5, model 0.73-LP-5 captured peak strength and overall hysteretic shape well, when compared to ECC-0.73-F (Fig. 9(b)). Peak strength of model 0.73-LP-5 was 3.5% less than that observed by ECC-0.73-F (Frank 2017). While model 0.73-LP-5 represented the hysteretic envelope of ECC-0.73-LP, it did not capture the energy dissipated as well as other models with respect to their associated experimental specimens. Model 0.73-LP-5 overestimated pinching due to the second of the two initial deformation pulses, which led to a 27% reduction in energy dissipated when compared to ECC-0.73-F. Pinching was qualitatively measured by observing the hysteretic loops, particularly the value of resistive force when the specimen cycled past zero drift. Models 0.95-F-5, 0.73-F-5, and 0.95-LP-5 all underpredicted the energy dissipation of their respective experimental specimens by 14%-17%, but the 27% difference in energy dissipated between model 0.73-LP-5 and ECC-0.73-LP could be partially attributed to the



(a) ECC-0.95-LP and 0.95-LP-5



(b) ECC-0.73-LP and 0.73-LP-5

Fig. 9 Hysteretic response

formation of an irregular dominant crack in ECC-0.73-LP, which the numerical model was unable to capture. The dominant crack on one side of ECC-0.73-LP formed in such a way that some amount of normal force was able to transfer across the dominant crack through bearing during excursions in one direction. Increased bearing across the dominant crack decreased the effect of pinching and increased energy dissipation in ECC-0.73-LP over that simulated with model 0.73-LP-5. Further evidence that an irregular crack may have increased energy dissipation in ECC-0.73-LP is slight asymmetry in the hysteresis loops. The minor asymmetry in the experiment resulted in the hysteresis envelope of model 0.73-LP-5 below the force axis ( $x$ -axis) to be in closer agreement than the hysteresis envelope above the force axis (Fig. 9(b)).

### 5.2.3 Steel reinforcement strain

Reinforcement strain profiles for models 0.95-LP-5 and 0.73-LP-5 were created during the respective simulations, however, none of the strain gages in experimental specimens ECC-0.95-LP or ECC-0.73-LP were functional beyond the initial pulses for use in model validation. The number of steel elements that strain-hardened, or incurred strain greater than yield strain, along the length of the steel reinforcement was similar on a numerical model reinforced to 0.95% steel reinforcement ratio when a simulated LP deformation history was imposed (Fig. 10) and when a simulated FEMA deformation history was imposed (Fig. 6).

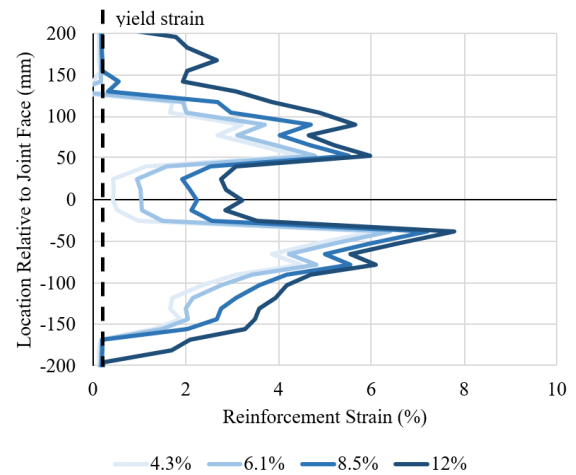


Fig. 10 Reinforcement strain profile in 0.95-LP-5

The main difference in reinforcement strain manifested by the LP deformation history relative to the FEMA deformation history was the reduction in reinforcement strain from about 40 mm into the joint to about 50 mm above the joint relative to the strain in the steel elements directly below and above. This 90 mm length of relatively low strain formed during the initial deformation pulses as the steel reinforcement debonded from the surrounding ECC material as bond demand exceeded bond strength. The initial deformation pulses facilitated reinforcement slip, which reduced bond strength, and led to a region of relatively low reinforcement strain. The region of relatively low reinforcement strain remained present throughout the duration of the simulation. This region of relatively low strain contributes to an understanding of how peak reinforcement strain may have been reduced by a large pulse. The relatively low reinforcement strain near the joint relieved strain accumulation from the initial deformation pulses at the location of the maximum moment demand. The simulated localized strain reduction supports experimental results from Frank (2017) and explains how ECC-0.95-LP and ECC-0.95-F experienced reinforcing bar fracture at the same drift (12% drift).

The profile of strain in the steel reinforcement in model 0.73-LP-5 (Fig. 11) was different than that of the same model subjected to the FEMA deformation history, model 0.73-F-5 (Fig. 7). Because the maximum cyclic amplitude (6.1% drift) in model 0.73-LP-5 was close to the amplitude of the initial deformation pulses (5.5% drift), the number of steel reinforcement elements that strain-hardened remained fairly constant from the first pulse through the conclusion of testing. The length of steel reinforcement in model 0.73-LP-5 that strain-hardened was about 220 mm at drifts of 3.1%, 4.3%, and 6.1% drift. For comparison to the model simulated with the FEMA deformation history, the length of steel reinforcement in model 0.73-F-5 that strain-hardened did not exceed a length of 220 mm until the first excursion to 12% drift (Fig. 7). In addition to the longer length of steel reinforcement elements that strain-hardened in model 0.73-LP-5 at drifts up until 6.1% drift, the maximum magnitude of reinforcement strain in model 0.73-LP-5 at all drifts was larger than that of model 0.73-F-5.

Table 3 Comparison of strain in the steel reinforcement at 12% drift between models subjected to the FEMA deformation history

Model	Peak reinforcement strain (%)			Length of reinforcing bar strain hardening (mm)		
	$k=-5.0$ MPa/mm	$k=-3.3$ MPa/mm	% difference	$k=-5.0$ MPa/mm	$k=-3.3$ MPa/mm	% difference
0.95-F-X	7.2	7.3	+1.4	390	364	-6.7
0.95-F-X	12	13	+7.7	260	240	-7.7

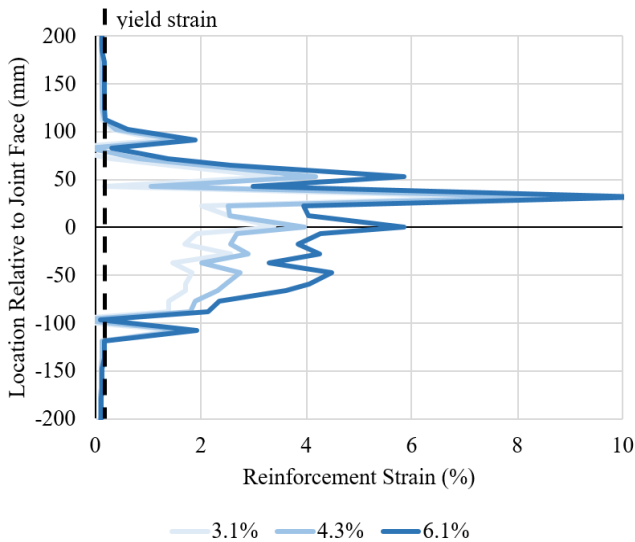


Fig. 11 Reinforcement strain profile in 0.73-LP-5

When comparing models of different reinforcement ratios subjected to the large pulse deformation history, unlike 0.95-LP-5, the reinforcement strain near the joint in model 0.73-LP-5 was not significantly lower relative to the strain in the steel just below or above the joint face. This lack of a reduction in strain near the location of maximum moment could be attributed to the initial pulse amplitude being lower or to a higher bond-strength-to-bond-demand ratio in model 0.73-LP-5 than model 0.95-LP-5. The steel reinforcement ratio and reinforcing bar size was lower in model 0.73-LP-5 than in model 0.95-LP-5. Higher bond-strength-to-bond-demand ratio provided a greater resistance to debonding of the steel reinforcing bar from the ECC. Greater resistance to debonding led to the increase in strain in the steel reinforcement elements with increasing drift within the plastic hinge region of model 0.73-LP-5 (Fig. 11).

Though reinforcing bar fracture could not be simulated with the reinforcement model formulation used, peak steel reinforcement strain may be compared between models, at the same drift, to provide an indication of proximity to failure since experimental failure occurred by fracture of the steel reinforcement. The peak strain in the steel reinforcement at the first excursion to 6.1% drift, for example, in models 0.73-LP-5 and 0.73-F-5 was 10% and 7.5%, respectively (Fig. 11 and Fig. 7). The aforementioned increase in peak strain in 0.73-LP-5 relative to 0.73-F-5 at 6.1% drift is commensurate with the lower ultimate drift experimentally observed in ECC-0.73-LP as compared to ECC-0.73-F as reported by Frank (2017).

### 5.3 Sensitivity of results to choice of bond-slip model

#### 5.3.1 FEMA deformation history

In models subjected to the FEMA deformation history, the post-peak bond-slip softening stiffness was reduced from  $-5.0$  MPa/mm to a more gradual slope of  $-3.3$  MPa/mm. The presence and location of a single dominant crack and the extent of multiple cracking along the height of the specimen did not change. There was no difference in peak force in either model 0.95-F-3 or model 0.73-F-3 when compared to model 0.95-F-5 and model 0.73-F-5, respectively. As expected, these results indicate peak specimen strength was not affected by post-peak response (i.e., selection of the parameter,  $k$ ).

Changes in total energy dissipated were negligible (4% increase in model 0.95-F-3 relative to model 0.95-F-5, and 2% increase in model 0.73-F-3 relative to model 0.73-F-5). For a given post-peak reinforcement slip, post-peak bond strength was higher when the softening slope was shallower ( $k=-3.3$  MPa/mm) than when the softening slope was steeper ( $k=-5$  MPa/mm). The higher bond strength facilitated more strain compatibility between the ECC and steel reinforcing bar elements during cycling, thus resulting in a slight increase in energy dissipation.

In general, strain in the steel reinforcement elements varied with the choice of post-peak bond-slip softening stiffness more than simulated cracking strains, peak force, and energy dissipated. For example, at 12% drift, peak reinforcement strain increased 7.7% when post-peak bond-slip softening stiffness changed from  $-5.0$  MPa/mm to  $-3.3$  MPa/mm when subjected to the FEMA deformation history and reinforced to 0.73% steel reinforcement ratio (Table 3). When  $k=-3.3$  MPa/mm, bond strength was higher for a given slip, which facilitated an increase in strain compatibility as measured by less slip between steel and ECC elements, as expected.

The increase in peak strain in the steel reinforcement as the parameter,  $k$ , was reduced from  $-5.0$  MPa/mm to  $-3.3$  MPa/mm was accompanied by a small decrease in the length of the bar that exceeded yield strain. This indicated that the region of steel plasticity became more concentrated as the magnitude of strain within that region increased. Plastic strain in the steel reinforcement at 12% drift decreased from a total length of 390 mm in model 0.95-F-5 to 364 mm in model 0.95-F-3 (Table 3). Between models reinforced to 0.73% steel reinforcement ratio and subjected to the FEMA deformation history, plastic strain in the steel reinforcement decreased from a total length of 260 mm to 240 mm at 12% drift between models 0.73-F-5 and 0.73-F-3. A more concentrated steel reinforcement strain with a larger peak magnitude is expected to lead to earlier fracture in a numerical simulation.

Table 4 Comparison of strain in the steel reinforcement at ultimate\* drift between models subjected to the LP deformation history

Model	Peak reinforcement strain (%)			Length of reinforcing bar strain hardening (mm)		
	$k=-5.0$ MPa/mm	$k=-10$ MPa/mm	% difference	$k=-5.0$ MPa/mm	$k=-10$ MPa/mm	% difference
0.95-LP-X	7.2	6.3	-13	325	390	+20
0.95-LP-X	10	7.5	-25	230	270	+22

\*ultimate drift was 12% and 6.1% drift for models 0.95-LP-X and 0.73-LP-X, respectively

### 5.3.2 LP deformation history

In models subjected to the LP deformation history, the post-peak bond-slip softening stiffness was changed from -5.0 MPa/mm to -10 MPa/mm to simulate a splitting crack which is expected to generate an abrupt post-peak strain reduction. Models reinforced to 0.95% and 0.73% steel reinforcing ratio were simulated as 0.95-LP-10 and 0.73-LP-10. As with the sensitivity of the models subjected to the FEMA deformation history, the location and extent of cracking, including the presence of a single dominant crack, did not change with the parameter,  $k$ . Additionally, there was no difference in peak force with changes in post-peak bond-slip softening stiffness at either steel reinforcement ratio, 0.95% or 0.73%, when subjected to the LP deformation history, as expected. Changes in the amount of total energy dissipated were negligible (2% decrease when comparing model 0.95-LP-10 to 0.95-LP-5, and 1% decrease when comparing model 0.73-LP-10 to 0.73-LP-5). For a given post-peak reinforcement slip, bond strength was higher when  $k=-5.0$  MPa/mm than when  $k=-10$  MPa/mm. The higher bond strength facilitated more strain compatibility between the ECC and the steel reinforcing bar elements during simulated cycling as identified by less slip, which increased energy dissipation.

Strain in the steel reinforcement elements varied significantly with bond-slip model in specimens subjected to the LP deformation history (Table 4). Changing the post-peak bond-slip softening stiffness from -5.0 MPa/mm to -10 MPa/mm reduced the peak strain in the steel reinforcement at 12% drift by 13% when the model was reinforced to 0.95% steel reinforcement ratio. When reinforced to 0.73% steel reinforcement ratio, the post-peak bond-slip softening stiffness had a greater effect, reducing the peak reinforcement strain in the steel elements at 6.1% drift by 25% in the model 0.73-LP-10 relative to 0.73-LP-5.

In conjunction with the aforementioned decrease in peak strain in the steel elements, the length of the steel reinforcement that exceeded yield strain increased as the parameter,  $k$ , changed from -5.0 MPa/mm to -10 MPa/mm. This indicated, as expected, that the region of steel plasticity increased in length as the peak value of strain in the steel reinforcement decreased. Plastic strain in the steel reinforcement elements increased 20% between models 0.95-LP-5 and 0.95-LP-10, at 12% drift (Table 4). Between models reinforced to 0.73% steel reinforcing ratio and subjected to the LP deformation history, the length of steel reinforcement that strain hardened at 6.1% drift increased 22% from model 0.73-LP-5 to model 0.73-LP-10. A more resilient bond between the reinforcing bar and the cementitious composite, indicated by a larger magnitude in the parameter,  $k$ , resulted in a higher peak reinforcement

strain and hardening concentrated along a shorter length of the reinforcing bar. This is consistent with observations from Moreno *et al.* (2014), Bandelt and Billington (2016a).

When  $k=-5$  MPa/mm, no reduction in steel reinforcement strain was observed near the joint relative to steel elements above or below the joint. However, when  $k=-10$  MPa/mm, local steel reinforcing strain maxima exist near -10 mm and 90 mm, and steel reinforcement strain was reduced in between. For a given reinforcement slip, post-peak bond strength was lower when  $k=-10$  MPa/mm than when  $k=-5.0$  MPa/mm. The lower bond strength facilitated bond degradation between ECC and steel reinforcing bar elements during the initial deformation pulses, and reduced values of steel reinforcing strain. Of the four simulations subjected to the LP deformation history, only model 0.73-LP-5 did not experience reinforcing bar strain reduction near the joint. Model 0.73-LP-5 contained a relatively high bond-strength-to-bond-demand ratio (0.73% steel reinforcement ratio) and a comparatively high post-peak bond-slip softening stiffness ( $k=-5.0$  MPa/mm), which limited the opportunity for bar slip and bond degradation, and reduced the tendency for the localized steel reinforcement strain reduction.

Changes in post-peak bond-slip softening stiffness affected the strain in the steel reinforcement elements in reinforced ECC numerical models with a lower (0.73%) steel reinforcement ratio more than models with a higher (0.95%) steel reinforcement ratio. This greater effect in models with a lower steel reinforcement ratio indicated specimens with a higher bond-capacity-to-bond-demand ratio were more sensitive to bond-slip models that alter post-peak bond strength than specimens with a lower bond-capacity-to-bond-demand ratio. With a lower bond-capacity-to-bond demand ratio, an increase in bond degradation occurred, reducing the impact of strain accumulation in the steel reinforcing bar elements due to loading cycles. With a greater bond-capacity-to-bond demand ratio, bond strength was preserved at increasing levels of reinforcing bar slip, and strain accumulation in the steel reinforcing bar elements was more sensitive to the number and amplitude of subsequent loading cycles. Results herein are in line with experimental results wherein only reinforced ECC specimens with a low steel reinforcement ratio experienced bar fracture at lower drifts when subjected to the LP deformation history than the FEMA deformation history (Frank 2017).

Further, the post-peak bond-slip softening stiffness,  $k$ , affected models subjected to the LP deformation history more than models subjected to the FEMA deformation history. This greater effect of the parameter,  $k$ , in conjunction with the LP deformation history indicated

deformation histories with greater cumulative cyclic deformation exacerbate the effect of variations in the bond-slip model.

## 6. Conclusions

Simulations of reinforced ECC flexural members were reported in this study using various steel reinforcement ratios, applied deformation histories, and post-peak bond-slip softening stiffness parameters. Cracking pattern and hysteretic response were not sensitive to the different bond-slip models in this study, but reinforcement strain was sensitive to the post-peak bond-slip softening stiffness parameter,  $k$ . The recommended value of the post-peak bond-slip softening stiffness for cyclic simulations in Bandelt (2015),  $k=-5.0$  MPa/mm, produced accurate cracking patterns, hysteretic behavior, and strain in the steel reinforcement for reinforced ECC flexural members with both 0.95% and 0.73% steel reinforcement ratio and subjected to both the FEMA and Large Pulse deformation histories.

Steel reinforcement strain was more sensitive to the bond-slip model as steel reinforcement ratio and reinforcing bar size decreased. With limited experimental strain data for use in model validation, it was difficult to deduce which bond-slip model better represented the experimental reinforcement strain gage data. However, based on these findings, a post-peak bond-slip softening stiffness of -5.0 MPa/mm proved sufficiently versatile across multiple steel reinforcement ratios and deformation histories.

Adjusting the post-peak bond-slip softening stiffness from -5.0 MPa/mm to -3.3 MPa/mm to simulate bond degradation due to interface crushing in specimens subjected to the FEMA deformation history produced negligible changes in cracking strains and hysteretic response. Similarly, adjusting the post-peak bond-slip softening stiffness from -5.0 MPa/mm to -10 MPa/mm to simulate bond degradation due to splitting cracks in specimens subjected to the LP deformation history resulted in negligible differences in cracking strains and hysteretic response. Additional bond-slip experiments in reinforced ECC or other fiber reinforced cementitious composites are required using various deformation histories to better understand the bond softening response.

Analyses of strain in the steel reinforcement from two-dimensional numerical simulations were able to offer a more comprehensive insight into what may have occurred in experimental testing of reinforced ECC beams reported in Frank (2017). Specifically, the length of reinforcing bar that strain hardened was shorter yet the maximum magnitude of strain was higher in specimens with a smaller steel reinforcement ratio. Additionally, large initial pulses generated reinforcing bar slip and led to strain reductions in the model reinforced to 0.95% steel reinforcement ratio. Simulated strain reductions in specimens reinforced to 0.73% steel reinforcement ratio were not observed numerically. Differences in simulated reinforcing bar strain profile and strain reduction as steel reinforcing ratio varied may have generated the decrease in ductility with the presence of initial pulses in experimental ECC beams

reinforced to 0.73% but not in specimens reinforced to 0.95% steel reinforcement ratio.

Sensitivity analyses to other bond-slip model parameters, such as peak or residual bond strengths, could be carried out as part of future work and compared to experimental results. Techniques to accurately predict reinforcing bar fracture would be valuable for design for collapse prevention. Future numerical simulations of reinforced ECC flexural members with a reinforcement ratio less than 0.73% would help validate the observation that initial deformation pulses do not cause bar slip in reinforced ECC beams with lower steel reinforcement ratios. Further, numerical simulations of reinforced ECC flexural members with a reinforcement ratio between 0.73% and 0.95% would investigate an upper bound of steel reinforcement wherein localized strain reduction is expected near the joint rather than strain accumulation as drift increases following large initial pulses.

## Acknowledgments

The authors would like to acknowledge financial support provided by the Air Force Institute of Technology, the John A. Blume Earthquake Engineering Center, and the Thomas V. Jones Engineering Faculty Scholarship at Stanford University. The views expressed in this dissertation are those of the author and do not reflect the official policy or position of the United States Air Force, Department of Defense, or the U.S. Government.

## References

- Bandelt, M.J. (2015), "Behavior, modeling, and impact of bond in steel reinforced high-performance fiber-reinforced cement-based composites", Ph.D. Dissertation, Stanford University, California.
- Bandelt, M.J. and Billington, S.L. (2016a), "Bond behavior of steel reinforcement in high-performance fiber-reinforced cementitious composite flexural members", *Mater. Struct.*, **49**(1), 71-86.
- Bandelt, M.J. and Billington, S.L. (2016b), "Impact of reinforcement ratio and loading type on the deformation capacity of high-performance fiber-reinforced cementitious composites reinforced with mild steel", *J. Struct. Eng.*, 04016084.
- Bandelt, M.J., Frank, T.E., Lepech, M.D. and Billington, S.L. (2017), "Bond behavior and interface modeling of high-performance fiber-reinforced cementitious composites", *Cement Concrete Compos.*, **83**, 188-201.
- Cunha, V.M.C.F., Barros, J.O.A. and Sena-Cruz, J.M. (2012), "A finite element model with discrete embedded elements for fibre reinforced composites", *Comput. Struct.*, **94-95**, 22-33.
- FEMA 461 (2007), Interim Testing Protocols for Determining the Seismic Performance Characteristics of Structural and Nonstructural Components, Applied Technology Council, Redwood City, CA, USA.
- Frank, T.E. (2017), "Response of reinforced engineered cementitious composite flexural members subjected to various cyclic deformation histories", Ph.D. Dissertation, Stanford University, California.
- Frank, T.E., Lepech, M.D. and Billington, S.L. (2017), "Experimental testing of reinforced concrete and reinforced

- ECC flexural members subjected to various cyclic deformation histories”, *Mater. Struct.*, **50**(232), 1-12.
- Frank, T.E., Lepech, M.D. and Billington, S.L. (2018), “Experimental testing of reinforced ECC beams subjected to various cyclic deformation histories”, *J. Struct. Eng.*, **144**(6), 04018052.
- Han, T.S., Feenstra, P.H. and Billington, S.L. (2003), “Simulation of highly ductile fiber-reinforced cement-based composite components under cyclic loading”, *ACI Struct. J.*, **100**(6), 749-757.
- Harajli, M., Hamad, B. and Karam, K. (2002), “Bond-slip response of reinforcing bars embedded in plain and fiber concrete”, *J. Mater. Civil Eng.*, **14**(6), 503-511.
- Hung, C.C. and El-Tawil, S. (2010), “Hybrid rotating/fixed-crack model for high-performance fiber-reinforced cementitious composites”, *ACI Mater. J.*, **107**(6), 568-576.
- Kaufmann, W. and Marti, P. (1998), “Structural concrete: cracked membrane model”, *J. Struct. Eng.*, **124**(12), 1467-1475.
- Kwak, H.G. and Filippou, F.C. (1990), “Finite element analysis of reinforced concrete structures under monotonic loads”, Technical Report, University of California, Berkeley Report No. UCB/SEMM-90/14, Berkeley, California.
- Leon, R.T. and Deierlein, G.G. (1996), “Considerations for the use of quasi-static testing”, *Earthq. Spectra*, **12**(1), 87-109.
- Li, V.C. and Kanda, T. (1998), “Engineered cementitious composites for structural applications”, *ASCE J. Mater. Civil Eng.*, **10**(2), 66-69.
- Maalej, M. and Li, V.C. (1995), “Introduction of strain-hardening engineered cementitious composites in design of reinforced concrete flexural members for improved durability”, *ACI Struct. J.*, **92**(2), 167-176.
- Moreno-Luna, D.M. (2014), “Tension stiffening in reinforced high performance fiber reinforced cement based composites”, Ph.D. Dissertation, Stanford University, California.
- Moreno, D.M., Trono, W., Jen, G., Ostertag, C. and Billington, S.L. (2014), “Tension stiffening in reinforced high performance fiber reinforced cement-based composites”, *Cement Concrete Compos.*, **50**, 36-46.
- Radtke, F.K.F., Simone, A. and Sluys, L.J. (2010), “A computational model for failure analysis of fibre reinforced concrete with discrete treatment of fibres”, *Eng. Fract. Mech.*, **77**(4), 597-620.
- Shen, C., Mizuno, E. and Usami, T. (1993), “A generalized two-surface model for structural steels under cyclic loading”, *Struct. Eng. Mech.*, **10**(2), 59-69.
- Soranakom, C. and Mobasher, B. (2007), “Closed-form solutions for flexural response of fiber-reinforced concrete beams”, *J. Eng. Mech.*, **133**(8), 933-941.
- Stavridis, A. and Shing, P.B. (2010), “Finite-element modeling of nonlinear behavior of masonry-infilled RC frames”, *J. Struct. Eng.*, **136**(3), 285-296.